An integrated approach for the systematic evaluation of polymeric nanoparticles in healthy and diseased organisms

Leopoldo Sitia · Katia Paolella · Michela Romano · Martina Bruna Violatto · Raffaele Ferrari · Stefano Fumagalli · Laura Colombo · Ezia Bello · Maria Grazia De Simoni · Maurizio D'Incalci · Massimo Morbidelli · Eugenio Erba · Mario Salmona · Davide Moscatelli · Paolo Bigini

Received: 21 March 2014 / Accepted: 23 May 2014 / Published online: 12 June 2014

L. Sitia · K. Paolella · M. Romano · M. B. Violatto · S. Fumagalli · L. Colombo · E. Bello · M. G. De Simoni · M. D'Incalci · E. Erba · M. Salmona · P. Bigini (✉)
IRCCS-Istituto di Ricerche Farmacologiche "Mario Negri", Via La Masa 19, 20156 Milan, Italy
e-mail: paolo.bigini@marionegri.it

R. Ferrari · M. Morbidelli · D. Moscatelli
Department of Chemistry, Materials and Chemical Engineering 'Giulio Natta', Politecnico di Milano, Via Luigi Mancinelli 7, 20131 Milan, Italy

S. Fumagalli
Neurosurgical Intensive Care Unit, Fondazione IRCCS Ca' Granda/Ospedale Maggiore Policlinico, Via Francesco Sforza, 33, 20122 Milan, Italy

M. Morbidelli
Institute for Chemical and Bioengineering, ETH Zurich, 8093 Zurich, Switzerland

Background

In the last decades, the application of material engineering in the biomedical field has generated a large amount of nanometric compounds for diagnostic and pharmacological uses (Parveen et al. 2011). One of the fields in which nanoparticles (NPs) have been mostly studied is oncology (Mukerjee et al. 2012; Peer et al. 2007). In spite of three decades of research on nanomaterials and the exceptional improvements that NPs might bring in cancer therapy (e.g., prolonged biodistribution, active target therapy, reduced toxicity, combined diagnosis and therapy), many obstacles have hampered the clinical development of nanodrugs. In fact, there are only very few NP formulations that are in clinic nowadays (Wang et al. 2011). Doxil®, doxorubicin-loaded liposomes, and Abraxane®, an albumin-based paclitaxel nanoformulation, are commonly used for the treatment of ovarian, breast, and lung cancers (Malam et al. 2009; Barenholz 2012; Ma and Mumper 2013). Other organic and inorganic nanomaterials have been proposed for drug delivery, including silica, metals, carbon nanostructures, and biopolymers (Matsumura 2008; Yang et al. 2013). The growing interest in polymers is related to their great plasticity, the possibility to "finely" tune their physico-chemical properties, their degree of functionalization, and their biocompatibility. The potential of polymeric NPs in improving the pharmacokinetics of loaded therapeutic molecules, enhancing their stability, making better targeted delivery, and reducing side effects has been demonstrated in different preclinical tumor models (Nazir et al. 2014). In particular, in a context where traditional chemotherapeutic strategies and target therapies (such as endocrine or anti-HER2 therapies) are proven unsuccessful, drug delivery might play a fundamental role. This is the case of triple-negative breast cancer (TNBC) where traditional strategies are greatly hampered by the concomitant absence of the three main receptors (estrogen, progesterone, and HER2) commonly expressed in breast tumors (de Ruijter et al. 2011). TNBC constitutes 10–20 % of all breast carcinomas, and it is characterized by a large size, frequent lymph node involvement, high aggressiveness, metastasis formation, and poor prognosis (Pal et al. 2011). NPs were already tested against TNBC, with promising results (Deng et al. 2013; Inoue et al. 2012).

Although the clear potentials of NP dependent drug delivery, the lack of detailed characterization of nanomaterials often obstacles a quick development toward more complex clinical investigations. Issues such as behavior in biological fluids, the interaction with target cells, toxicity, and the pharmacokinetics in healthy and diseased animals should be carefully studied. Highly standardized and uniform systems of analysis should be developed to categorize the impact of nanocarriers before their development for pharmacological purposes (Akhter et al. 2013; De Jong and Borm 2008).

The present study stems from the need to fill this lack. To this aim we generated an integrated platform focused at elucidating the mutual influence between polymeric nanomaterials and preclinical models of TNBC at increasing levels of complexity (biological fluids, cells, healthy and pathological organisms). Initially, we studied how physico-chemical properties regulate NP-biological fluids interaction and influence NP cellular uptake, subcellular localization, cytotoxicity, proliferation, and cell cycle in two different lines of TNBC. Finally, we studied NP permanence into the bloodstream, tissue biodistribution, progressive clearance in filter organs, and the active migration in tumor parenchyma in mice. Because of their high stability, finely tuned poly(methyl methacrylate) NPs (PMMA-NPs) were used to set the platform (Ferrari et al. 2014). To integrate in vitro, in vivo, and ex vivo imaging, PMMA-NPs were labeled with two fluorophores rhodamine-B (RhB) and a deep infrared dye (DIR). The platform that is here described appears suitable for the screening and selection of NPs that could be used as delivery systems for a variety of compounds that can be potentially effective against resistant tumors such as our TNBC models (Liechty and Peppas 2012).

Materials and methods

Synthesis and characterization of fluorescent PMMA-NPs

To generate fluorescent macromonomer of 2-hydroxyethyl methacrylate (HEMA) covalently bound to RhB, *N*,*N*′-dicyclohexylcarbodiimide (DCC) was used as an esterification agent with DMAP as a catalyst (Cova et al. 2013; Dossi et al. 2012). This fluorescent macromonomer (HEMA-RhB) was further copolymerized with a controlled amount of methyl methacrylate (MMA) and RhB to generate stable and uniform

NPs. The reaction was run in acetonitrile and details on synthesis-characterization are reported in the Supporting Information (SI, Figs. S1, S2). PMMA-NPs were synthesized through an emulsion-free radical copolymerization process between MMA and HEMA-RhB (0.01 % wt/wt in respect to MMA) (Ferrari et al. 2014) to ensure narrow particle size distribution as described in SI. To produce positively and negatively charged NPs 2,2′-Azobis(2-methyl-propionamidine) dihydrochloride and potassium persulfate (KPS) were used as initiators, respectively. Reactions were performed in batch emulsion polymerization (BEP) or in monomer-starved semi-batch emulsion polymerization (MSSEP).

The following parameters were used to synthesize NPs with different sizes and surface charges:

- Positive 50 nm PMMA-NPs (PMMA-50^{+}): 2 g MMA and 20 % Tween80/MMA, in MSSEP.
- Positive 100 nm PMMA-NPs (PMMA-100^{+}): 2.5 g MMA and 20 % Tween80/MMA, in BEP.
- Positive 200 nm PMMA-NPs (PMMA-200^{+}): 2.5 g MMA and 5 % Tween80/MMA, in BEP.
- Negative 50 nm PMMA-NPs (PMMA-50^{-}): 2 g MMA and 35 % Tween80/MMA, in MSSEP.
- Negative 100 nm PMMA-NPs (PMMA-100^{-}): 2 g MMA and 15 % Tween80/MMA, in MSSEP.
- Negative 200 nm PMMA-NPs (PMMA-200^{-}): 2.5 g MMA and10 % Tween80/MMA, in BEP.

Deep infrared dye (DIR) was not loaded during NPs formation due to high temperature and to the presence radicals; therefore a post-synthesis process has been adopted. DIR was dissolved in DMSO at a concentration of 0.05 mg/ml and entrapped in the pre-formed NPs. 4-h dialysis against PBS was employed to remove unloaded DIR.

Average NP size was measured using dynamic light scattering (DLS, Zetanano ZS, Malvern) in dH_2O using Micro UVCuvettes, $12.5 \times 12.5 \times 45$ mm^3 (70 μL) with light path 1 cm (Brand GmbH). Further characterization to prove the incorporation of RhB into the polymer matrix is reported in the SI (Figs. S3, S4).

Transmission electron microscopy, atomic force microscopy, and fluorimetry

The morphology of NPs of different sizes was first observed by transmission electron microscopy. TEM analyses have been performed using a 200 kV electron microscope (Philips CM200-FEG) and preparing the sample drying a drop of NP latex on a copper grid coated with a carbon film (Cu-grid 200 Mash). The stability of NP (in terms of dispersity and shape maintenance) was assessed in dH_2O and after 48 h of incubation with human serum by atomic force microscopy (AFM, NanoscopeV, Veeco instruments, Plainview, NY USA) as previously described (Albani et al. 2009). To clarify the behavior of the fluorophores internalized in NPs and the possible interference signal in these biological fluids, NP fluorescence properties were analyzed through fluorimetry (multimode plate reader Infinite® M200) (Ferrari et al. 2014).

Cell lines and culture conditions

For in vitro studies we used two TNBC cell lines; the murine 4T1 and the human MDA-MB231.1833. 4T1 cells were grown in monolayer in Ham's F12 supplemented with 10 % FBS and 1 % L-glutamine (200 mM). MDA-MB231.1833 cells were maintained in DMEM-high glucose supplemented with 10 % FBS and 1 % L-glutamine (200 mM).

Both cell lines were maintained at 37 °C in a humidified atmosphere at 5 % CO_2 in T25 or T75 flasks.

NP cellular internalization

4T1 and MDA-MB231.1833 cells were seeded on round glass slides in 24-well plates at the concentration of 2,000 cells/ml and 10,000 cells/ml, respectively, and left in adhesion for 24 h (Ferrari et al. 2014). Cells were incubated with positively and negatively charged 50, 100, and 200 nm PMMA-NPs for 6, 24, and 72 h and fixed with 4 % paraformaldehyde in PBS for 40′. Nuclei were stained with Hoechst-33258 (2 μg/ml in PBS) for 40′. Samples were then mounted on glass cover slides with Fluormount mounting medium and analyzed with an Olympus Fluoview microscope BX61 with confocal system FV500 equipped with specific lasers $\lambda exc = 405$ nm, $\lambda exc = 546$ nm for Hoechst-33258 and RhB, respectively. Quantitative evaluation of fluorescent markers indicating NP cellular interactions and uptake was performed through a specific image cytometry software (TissueQuest,

TissueGnosticsGmbH, Austria) as previously reported (SI, Fig. S5) (Cova et al. 2013).

To evaluate if serum influences NP-internalization, cells were treated with PMMA-100$^+$ pre-incubated in human serum for 48 h and compared with cells treated with PMMA-100$^+$ in dH_2O. 6, 24, and 48 h after NP incubation cells were fixed and analyzed as previously described.

Growth inhibition

Cell growth rate was evaluated incubating exponentially growing 4T1 and MDA-MB231.1833 cells with PMMA-NPs at three different concentrations. The original NP solutions were diluted to obtain final polymeric concentrations of 25, 50, and 100 μg/ml. Using the formula reported by our group (Ferrari et al. 2014), it was calculated that these absolute concentrations corresponded to nominal concentration of: 1.0×10^{11}, 2.0×10^{11}, and 4.0×10^{11} NPs/ml for PMMA-50$^+$; 0.5×10^{11}, 1.0×10^{11}, and 2.0×10^{11} NPs/ml for PMMA-100$^+$; 0.05×10^{11}, 0.10×10^{11}, and 0.25×10^{11}NPs/ml for PMMA-200$^+$. Cells were counted 24, 48 and 72 h after incubation using a Coulter Counter Multisizer 3 (Beckman Coulter, Inc.).

FACS analyses

At 24, 48, and 72 h after incubation with PMMA-100$^+$, at the three different reported concentrations, MDA-MB231.1833 cells were fixed in 70 % ethanol and the DNA was stained overnight with 1 ml of a solution containing (12.5 μg/ml) propidium iodide (PI) and 12.5 μl of RNAse (1 mg/ml). Flow cytometric analysis was done on at least 10,000 events for each condition using a FACS Calibur instrument (Becton–Dickinson, Sunnyvale, CA, USA). The determination of the cell proliferation rate was carried out by biparametric BrdU/DNA analysis as described in SI.

A cell membrane permeability assay was done to evaluate the mechanism of cell death induced by PMMA-100$^+$ on 4T1 and MDA-MB231.1833 cells by Vybrant® Apoptosis Assay (Molecular Probe).

Sub-localization

Cytoplasm immunohistochemistry assays were done to observe the distribution of PMMA-100$^+$ inside cells. We used vital dyes and antibodies labeled with fluorochromes to highlight the different cell organelles, including mitochondria (MitotrackerGreen®), early lysosomes (anti-Lamp II antibody), endosomes (anti-M6PR antibody), Golgi apparatus (anti-GM130 antibody) as described in SI.

Animals

Female athymic Foxn1 nu/nu mice, 6–8 weeks old, were obtained from Harlan Laboratories (Bresso, Italy). Mice were maintained under specific pathogen-free condition in the Institute's Animal Care Facilities; they were regularly checked by a certified veterinarian who is responsible for health monitoring, animal welfare supervision, and experimental protocol revision. Procedures involving animals and their care were conducted in conformity with the institutional guidelines at the IRCCS—Istituto di Ricerche Farmacologiche "Mario Negri" in compliance with national (Decreto Legge nr 116/92, Gazzetta Ufficiale, supplement 40, February 18, 1992; Circolare nr 8, Gazzetta Ufficiale, July 14, 1994) and international laws and policies (EEC Council Directive 86/609, OJL 358, 1, Dec. 12, 1987; Guide for the Care and Use of Laboratory Animals, US National Research Council, 8th edition, 2011). This project of research has been reviewed by IRCCS-IRFMN Animal Care and Use Committee (IACUC) and then approved by the Italian "Istituto Superiore di Sanità" (code: 17/01 D Appl 3).

In vivo and ex vivo fluorescence imaging

Biodistribution of PMMA 100$^+$ was studied in mice ($n = 8$) subcutaneously injected with 1×10^7 MDA-MB231.1833 cells. Two animals were treated with a physiological solution. Remaining animals were treated intra-vein with 200 μl of NPs ($1. \times 10^{13}$ NPs/ml). In vivo imaging was conducted on animals anesthetized with a continuous flow of 5 % isoflurane/oxygen mixture, just before NP administration (to set proper laser parameters avoiding non-specific autofluorescence signal) 2, 24, and 72 h after injection using Explore Optix System (ART Advanced Research Technologies, Montreal, Canada) as already described by our group (Bigini et al. 2013). For fluorescence analysis of single organs, two animals per scheduled time point were sacrificed. Liver, spleen, kidney, and tumor were explanted and imaged ex vivo with the Explore Optix System.

Two-photon in vivo microscopy

Mice were prepared for in vivo imaging by skull thinning craniotomy as already reported by our group (Fumagalli et al. 2011, 2013) and widely described in SI.

Histological analysis

Histological studies were performed in two experimental groups, perfused and non-perfused animals. NP biodistribution was followed for 2, 24, and 72 h after administration. All animals were deeply anesthetized with an overdose of ketamine (75 mg/kg)-medetotimine (1-mg-kg). The first group was transcardially perfused [4 % paraformaldehyde (w/v) in 0.1 M phosphate-buffered saline pH 7.4]. Liver, kidneys, spleen, and tumor were removed, postfixed in 4 % paraformaldehyde for 24 h and transferred to a 30 % sucrose solution until cryostat sectioning. In the second group, organs were immediately frozen in dry ice after sacrifice and stored at −80 °C until use. For both groups, 30-µm-thick serial sections of each organ were collected and stained with Hoechst 33258 (2 µg/ml in PBS, 35′, RT) for nuclei visualization. The slides related to perfused animals were visualized by confocal microscope, as previously described, while the sections derived from non-perfused animals were acquired with Nanozoomer HT 2.0 (Hamamastu Photonics, Hamamatsu City, Japan) scanner to obtain rapid scans of the organs in their whole volume, with high anatomical resolution.

Data calculation and statistical analysis

All data were expressed as mean ± S.D. Two-way ANOVA or Student's *t* test were used. *p* values ≤0.05 were considered significant. All statistical analyses were done using the Graph Pad Prism version 6.00 for Windows (Graph-Pad Software, San Diego, CA, USA).

Results

In vitro platform

The platform was set by a cluster of finely tuned PMMA-NPs of different dimensions and surface charges. We synthesized NPs of 50, 100, and 200 nm with positive and negative ζ-potential (SI, Fig. S6). Dynamic laser light scattering highlighted PMMA-NP stability indH_2O, saline solution, and culture medium for at least 2 weeks after incubation at 37 °C. All these parameters were maintained independently on the size or the external charge of NPs (SI, Fig. S6).

The analysis of PMMA-NP morphology done with TEM confirmed both the spherical shape of newly synthesized NPs and the average dimension measured

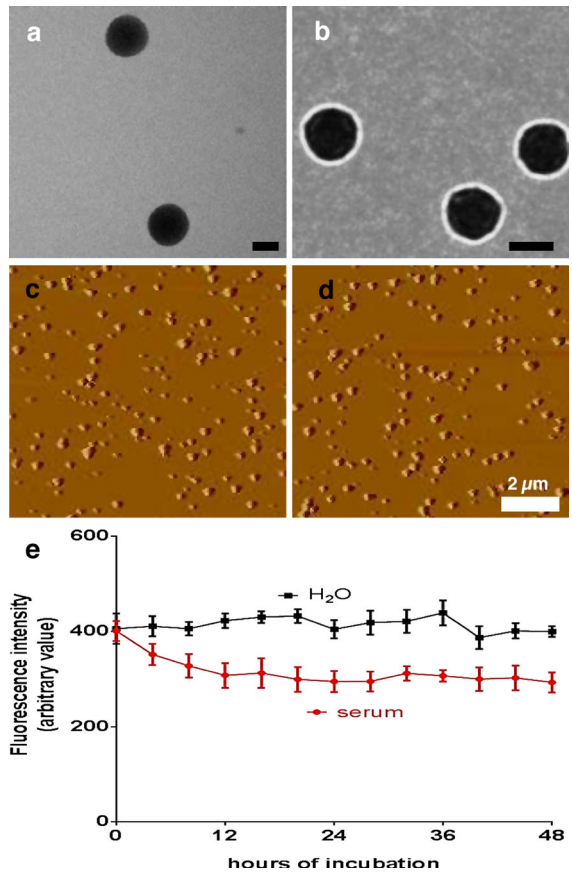

Fig. 1 Panels **a**, **b** Representative TEM images of PMMA NPs (PMMA-50^+ and PMMA-100^+ respectively) showing their shape and morphology. NPs result spherical and monodispersed. AFM analysis shows representative patterns of distribution of PMMA-100^+ in distilled water (**c**) or after 48 h incubation with human serum (**d**). This analysis confirms the stability of the selected NPs. *Scale bars* panel **a** = 50 nm; panel **b** = 100 nm; panel **c**, **d** = 2 µm. Panel **e** longitudinal analysis of the fluorescence intensity of PMMA-100^+ incubated with dH_2O (*black*) or human serum (*red*). Data are the mean ± SD of five independent measurements. Statistical analysis was done by two-way ANOVA (with Bonferroni post-test). (Color figure online)

with DLS analysis (Fig. 1a, b). Stability was then examined with AFM in dH_2O and after 48 h of NP incubation in human serum at 37 °C to understand if plasmatic proteins may influence their main physico-chemical parameters. Neither relevant changes in size and aggregation nor shape deformation were observed (Fig. 1c) compared to NPs suspended in dH_2O (Fig. 1d). Moreover, a fluorimetric analysis was performed to evaluate any influence of serum incubation on NP fluorescence emission over time. Even if the absolute fluorescence intensity seems slightly reduced by the presence of serum, the general trend of emission is comparable in the two conditions. The statistical analysis confirmed that the observed reduction is not statistically significant for the whole duration of the experiment (Fig. 1e). The lack of a significant quenching effect is vital for efficient visualization of NPs in in vitro and in vivo long term studies.

Following the characterization analyses that confirmed the stability of our PMMA-NPs, we then tested NP interactions with two different cell lines of TNBC. In particular we focused our attention on uptake ability, on NP-related toxicity and on the subcellular interactions. Fig. 2a shows the profile of NP internalization (red) 24 h after incubation with 4T1 cells (nuclei in blue). Quantitative data (Fig. 2b) confirmed that charge has an effect on NP cellular internalization. Positively charged NPs have higher uptake rates than negatively charged ones, and this effect was particularly evident for PMMA-100^+. Figure 2c, d suggests that the NP internalization considerably differed between the two TNBC models. In particular, from the quantitative analysis performed with TissueQuest, both the intracellular fluorescence intensity (Fig. 2e) and the percentage of cells internalizing PMMA-NPs (Fig. 2f) resulted significantly higher in 4T1 cells than MDA-MB231.1833.

We previously showed that serum incubation did not modify physico-chemical properties of NPs. However, serum pre-incubation significantly increased 4T1 cells NP entry (SI, Fig. S7) thus suggesting a relevant influence of plasmatic proteins in this process of uptake.

Since the optimization of NP cellular uptake is pivotal to design NP for intracellular drug delivery, we selected positively charged NPs for next studies.

We further investigated how PMMA-NPs interact with 4T1 cells by evaluating their subcellular localization at three different times (6, 24, and 72 h incubation). Representative staining of nuclei (blue) and different subcellular markers (green) 24 and 72 h after PMMA-100^+ incubation (red) are depicted in Fig. 3a. First column shows that the actin staining did not change over time. The increased yellow staining observed in merged images 72 h after NP incubation is merely due to the overlap of green and red signal (actin and internalized NPs, respectively). No change in the immunoreactivity of a Golgi apparatus marker (GM130) was observed at both time-points (Fig. 3a, second column). The increased merged signal (yellow) observed 72 h after incubation is most likely due to the progressive transport of internalized NPs from the periphery to the perinuclear region. On the contrary, a marked increase of the early endosomal marker M6PR immunoreactivity (Fig. 3a, third column, green signal) was found after 24 and 72 h of incubation. The increased expression of a mature lysosomes marker confirmed the activation of clearance mechanisms in response to the massive NP entry (Fig. 3a, right column). Quantitative data of fluorescence staining revealed that the progressive entry of NPs induced a fast increase of early lysosomes followed by an increase associated with low pH lysosomes in both TNBC lines. No statistical alterations of fluorescence were recorded for structural markers (cytoskeleton, Golgi apparatus, nucleus, mitochondria) at different time-points after NP incubation (Fig. 3b).

Experiments of growth rate, viability, replication, and cell-cycle were done to unveil possible dose- and/or time-dependent NP-toxicity. No significant difference in cell growth was observed depending on either NP size or on concentration and exposure time in 4T1 cells (Fig. 4a–c).

On the other hand, a significant reduction was observed in MDA-MB231.1833 at the latter time-point (48 h) independently from concentration (Fig. 4d–f). To better investigate this effect, the percentage of MDA-MB231.1833 cells expressing either apoptotic and/or necrotic markers was measured at basal conditions and after PMMA-100^+ incubation. A little but not significant increase of apoptotic markers (YO-PRO^+ cells) was found 24 h after NP administration, independent of their concentration (SI, Fig. S8). The rate of proliferating cells ($BrdU^+/BrdU^-$ cells) was slightly lower after NP exposure (SI, Fig. S9b). However, no significant changes in cell cycle phases were found at different time-points among all experimental groups (SI, Fig. S9a). These results suggest a strong tolerance of cells to PMMA-NPs at this experimental conditions.

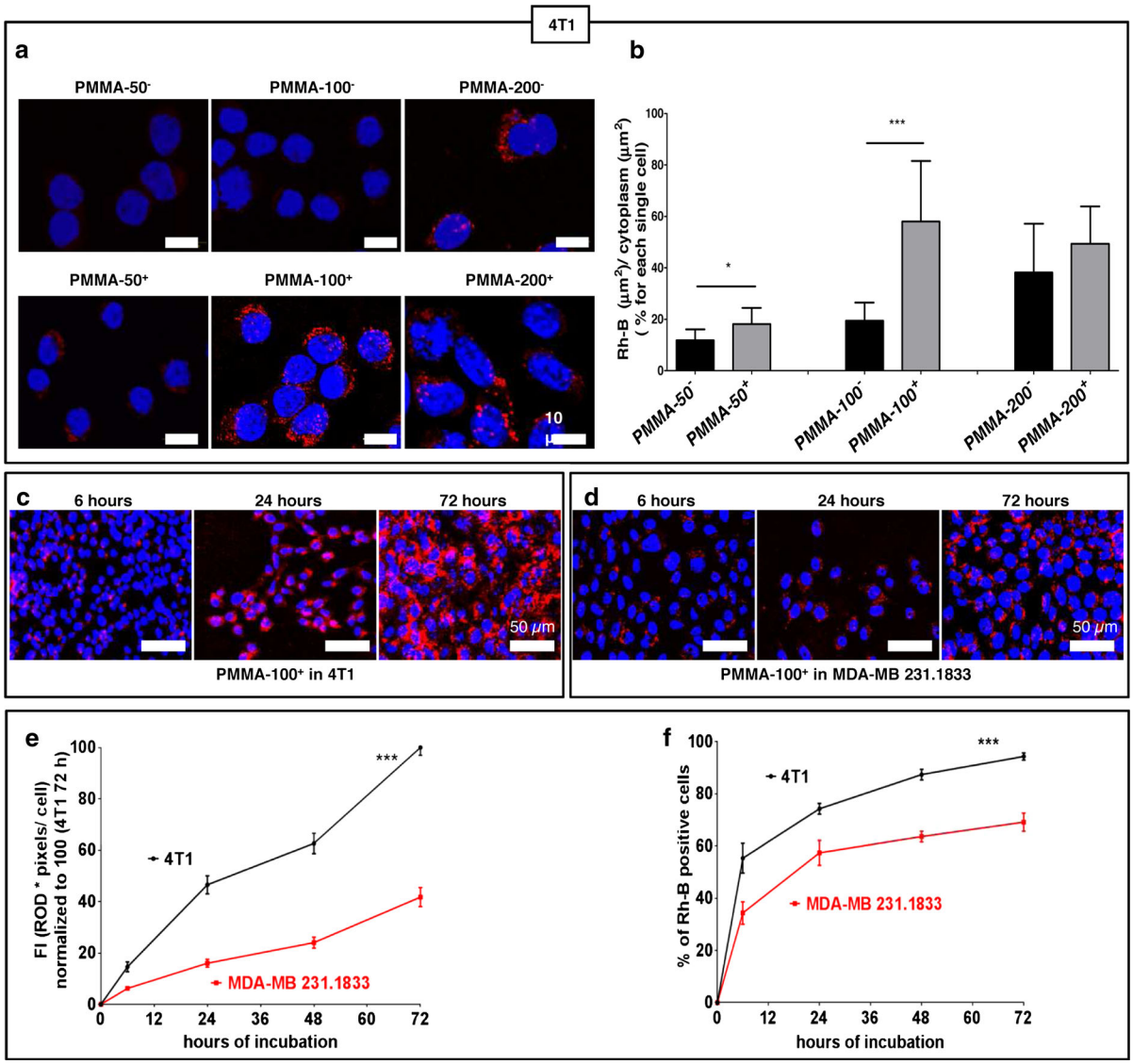

Fig. 2 **a**, **b** Representative confocal microscopy images showing internalization of different PMMA-NPs (*red signal*) in 4T1 cells (nuclei, *blue signal*) after 24 h of incubation (**a**) and relative quantitative analysis (**b**). *Histograms* show the spread of positively (*black bars*) and negatively charged PMMA-NPs (*gray bars*) inside the cells. Data are represented as mean ± SD from six different independent measurements for each experimental condition. $*p < 0.05$, $*p < 000.1$ higher than negatively charged PMMA-NP (unpaired Student's *t* test). **c**, **d** Representative pictures showing the kinetics of internalization of PMMA-100^+ in 4T1 (**c**) and MDA-MB231.1833 cells (**d**). **e**, **f** *Diagrams* showing the percentage of 4T1 (*black line*) or MDA-MB231.1833 cells (*red line*) internalizing PMMA-100^+ (**e**) and of the intensity of fluorescence for each cell (**f**). All data are expressed as mean ± SD of six independent measurements. Analysis was performed by two-way ANOVA (with Bonferroni post-test). $***p < 0.001$ difference from 4T1 and MDA-MB231.1833. (Color figure online)

In vivo, ex vivo platform

Longitudinal tracking of NP biodistribution was carried out by in vivo optical imaging after PMMA-100^+ systemic administration (Fig. 5a). The first panel shows the lack of any signal before NP injection. 2 h after NP administration, a strong signal was found in the upper-left side of abdomen (likely associated with liver and spleen) with a weaker fluorescence in correspondence to the renal region (Fig. 5a, second panel). One day after administration, no relevant alteration was observed in abdominal area whereas the

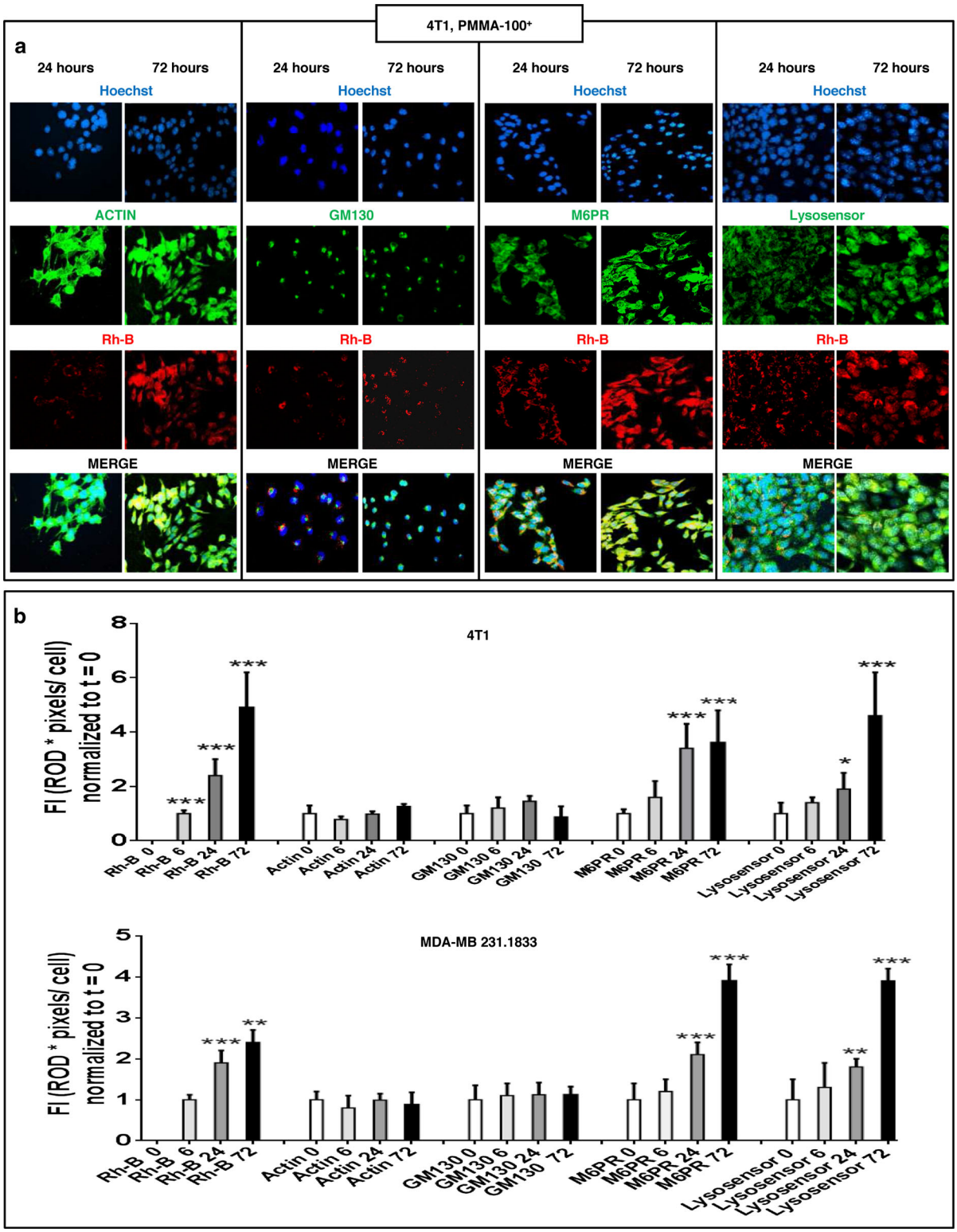
a
4T1, PMMA-100+
24 hours
72 hours
Hoechst
ACTIN
GM130
M6PR
Lysosensor
Rh-B
MERGE
b
4T1
MDA-MB 231.1833
FI (ROD * pixels/ cell) normalized to t = 0
Rh-B 0
Rh-B 6
Rh-B 24
Rh-B 72
Actin 0
Actin 6
Actin 24
Actin 72
GM130 0
GM130 6
GM130 24
GM130 72
M6PR 0
M6PR 6
M6PR 24
M6PR 72
Lysosensor 0
Lysosensor 6
Lysosensor 24
Lysosensor 72

◀**Fig. 3** **a** Representative confocal microscopy images of 4t1 cells incubated with PMMA-100^{+} showing expression of Hoechst-33258 (*upper line-blue*), subcellular markers (*second line-green*) NP (*third line-red*), and relative merge signal (*fourth line*). **b** Quantitative levels of fluorescence for different markers in 4T1 and MDA-MB231.1833 cells exposed to PMMA 100^{+} for 0, 6, 24 and 72 h. The mean fluorescence for RhB was normalized to 1 at $t = 6$ h. For other markers, fluorescence intensity was set as 1 at $t = 0$. Values are expressed as mean ± SD of twelve independent measurements. Analysis was done by unpaired Student's t test $^{**}p < 0.05$, $^{***}p < 000.1$ compared to the previous time-point. (Color figure online)

signal associated with renal system completely disappeared (Fig. 5a, third panel). A strong reduction of the signal, that remains high only in the epigastric region, was observed 72 h after administration (Fig. 5a, right). No signal associated with tumors was ever found during total body scanning acquisitions. However, when we repeated the scan on specific ROIs excluding the abdominal region, we found a lower but specific fluorescent signal associated to NPs accumulation into the tumor mass (Fig. 5c).

Ex vivo optical imaging confirmed the presence of NPs in filter organs and tumors at different time-points after NP administration (Fig. 5b). A rapid increase of signal was found in liver already 2 h after administration; then, NP fluorescence remained stable up until the 24th hour before slightly decreasing. In spleen, the trend of accumulation was similar to that observed in liver even if less intense. In kidneys, the signal was weaker and did not change overtime (no NPs accumulation). Even if different times lower than in liver, NP signal was also detectable in tumors where it reached its maximum intensity only 24 h after treatment with a slower kinetic of accumulation compared to other filter organs, where the maximum was observed 2 h after administration.

Two-photon confocal microscopy was carried out to visualize the presence of NPs in the bloodstream. Representative images of the brain cortical vasculature confirmed the presence of NPs in the vessels 30′ after administration (Fig. 6a). The speed and direction of the blood flow measured by calculating the slope of the non-fluorescent streaks (RBC speed) (Schaffer et al. 2006) confirmed the circulation of NPs in both small arterioles (Fig. 6a, vessel 1, RBC speed 1.143 mm/sec) and in big pial vessels (Fig. 6a, vessel 2, RBC speed 4.662 mm/sec). One day after injection the presence of NPs in the bloodstream, even if decreased, was still visible (Fig. 6b). Moreover the 3D reconstruction confirmed that NPs were closely confined into the circulatory tree (Fig. 6c).

Representative histological images of filter organs and tumors after blood removal are depicted in Fig. 6d. Very interestingly the quantification of the signal showed a fast NP accumulation in liver and spleen, with a fluorescence peak measured 24 h after administration that was maintained until the last time point. In tumor sections, NP accumulation was slower and the maximum intensity was reached only 72 h after administration. The presence of NPs was nearly absent in kidneys thus suggesting that these large NPs were not able to be efficiently uptaken by renal parenchyma (Fig. 6e).

To verify the actual contribution of NP in the resident blood, microscopy analyses of frozen not washed sections were carried out. Representative liver sections of animals sacrificed 1 and 24 h after NP injection are shown in Figs. 7a, c. One hour after administration, it is possible to notice that NPs are almost completely confined into the blood vessels. The higher magnified picture unveils the structure of the vessels and shows that NPs are both around the perimeter of the endothelium and inside blood cells. The pattern of fluorescence is completely different 24 h after administration (Fig. 7c) when NPs progressively migrate in parenchyma. A similar pattern was found in tumor sections (Fig. 7b, d). One hour after their administration, NPs were mainly confined in the vessels and on the external lamina of the tumor (Fig. 7b) whereas a widespread red signal was observed one day after NP administration (Fig. 7d, left).

These results demonstrate that, combining both in vivo and ex vivo techniques of analysis, our system allowed us to easily study NP biodistribution and define the kinetics of NP migration from the bloodstream to the parenchyma of target tissues.

Discussion

In the last decades, a growing number of studies have described the therapeutic potentials of nanomedicine in a wide variety of applications. In spite of these encouraging results, the translation from preclinical models to clinical practice has been nearly absent and a new generation of nanodrugs other than Doxil and Abraxane has not yet emerged. One of the reasons of

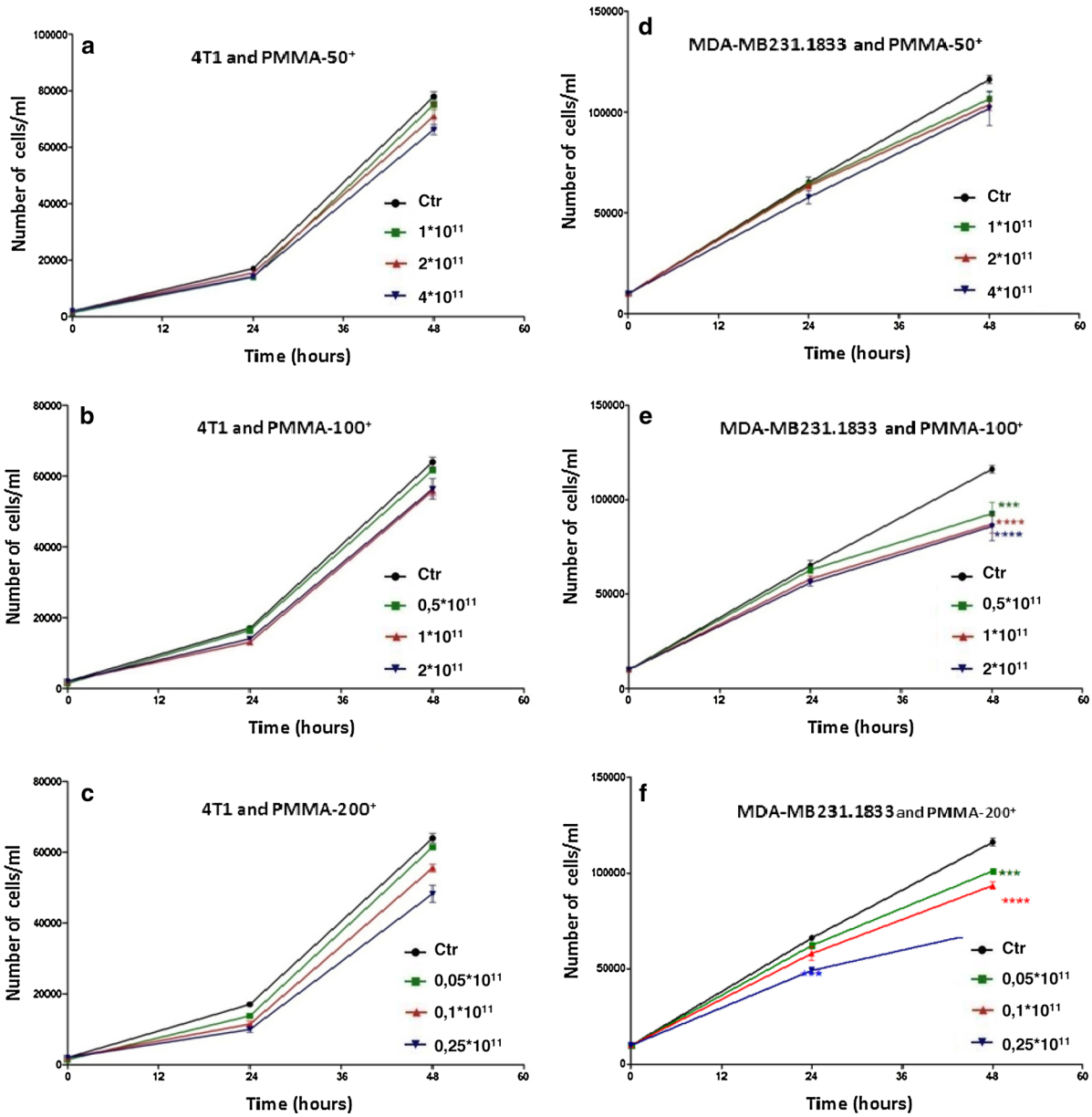

Fig. 4 Growth inhibition curves in 4T1 (**a**–**c**) and MDA-MB231.1833 cells (**d**–**f**) exposed to different concentrations of PMMA-50^{+}, PMMA-100^{+} and PMMA-200^{+}. *Black lines* indicate control cells; *green*, *red* and *blue lines* indicate the lowest, the intermediate and the highest NP concentration with which cells were incubated. All values are mean ± SD of three independent analyses. Analysis was done by two-way ANOVA (with Bonferroni post-test). ***$p < 0.001$ difference from untreated cells. (Color figure online)

this apparent dichotomy between basic science and clinical application is the lack of a careful characterization of the newly synthesized nanomaterials (Dobrovolskaia and McNeil 2013). Particular emphasis should be put in studying their safety, biocompatibility, and tropism to target tissues and/or cells. A standardized and integrated in vitro and in vivo system studying biological interactions at different stages of complexity (Cho et al. 2013) would be a reliable starting point to screen the potential of nanomaterials in nanomedicine. To this aim, a multimodal platform has been developed in this work. The main steps that

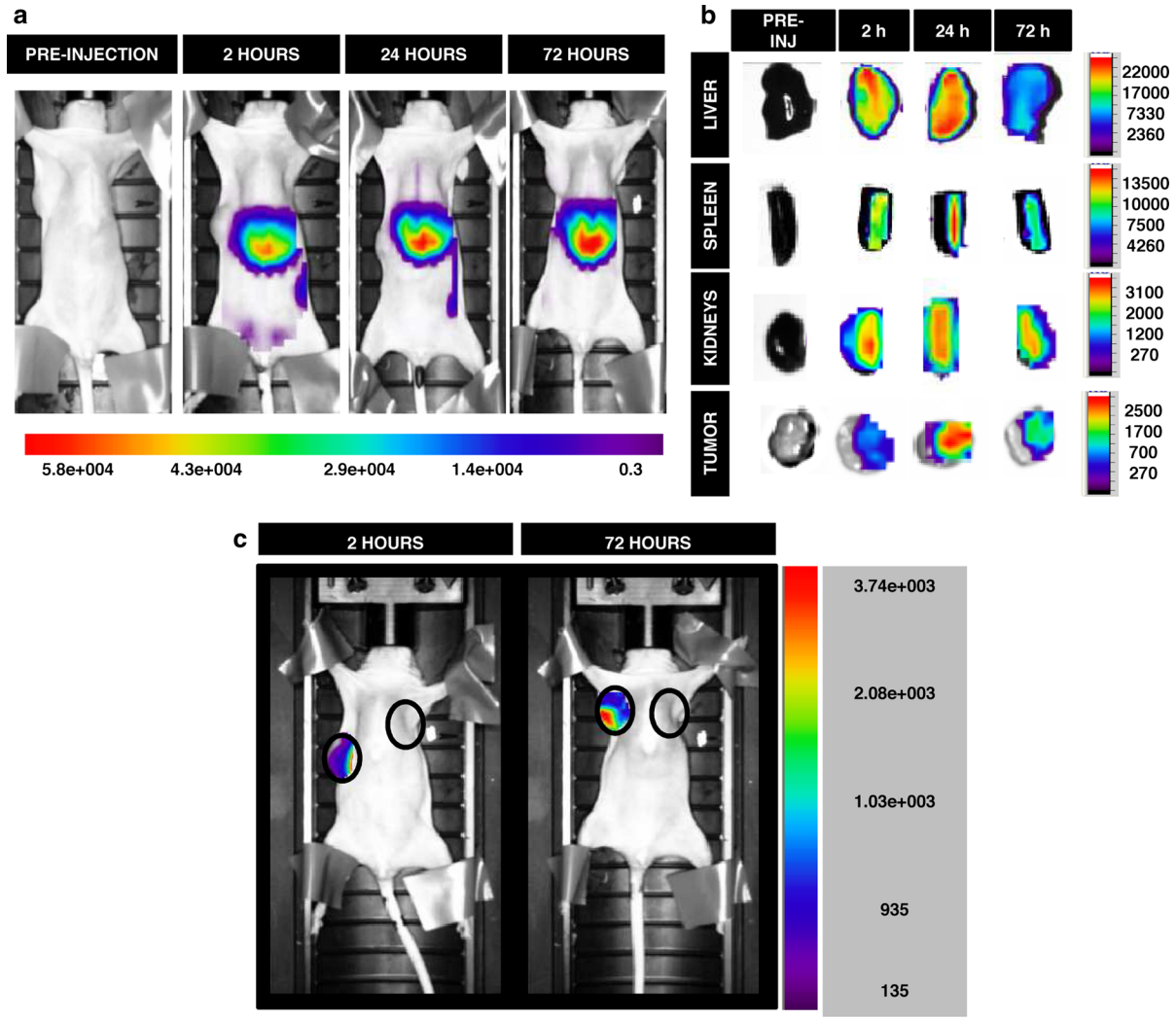

Fig. 5 **a**, **b** Representative optical imaging scans (**a**) showing the biodistribution of i.v. injected PMMA-100^{+} in tumor bearing mice and relative ex vivo scans of excised organs (**b**) at three different time-points after NP administration and before injection, in order to set acquisition parameters. **c** In vivo optical imaging scanning of the tumor area and of the controlateral side 2 h (*left*) and 72 h (*right*) after i.v. administration. The intensity of fluorescence signal, measured as normalized photon counts (NC), is shown as a *pseudo-color scale bar*. (Color figure online)

we included in our system and the relative results obtained are summarized in Tables 1 and 2.

Although our platform can be applied for a wide range of nanodevices, here we focused the attention on a single material (PMMA) and on a single therapeutic aspect (TNBC).

Before dwelling on the biological relevance of the platform, we would like to emphasize that, thanks to its flexibility, our system might be easily enriched when approaching different scenarios than the one presented here. Our system can be seen as a box that can be improved by inserting or removing modules without changing the effectiveness of the strategy. The creation of this box is "per se" a big novelty and a useful tool for the categorization of the impact of nanomaterials through a reproducible and well defined approach.

The first requirement to develop reliable nanomaterials for future clinical use is the synthesis of stable, pure, and highly reproducible NPs. These properties should not only be studied at the basal condition, but also in more complex biological systems, such as after

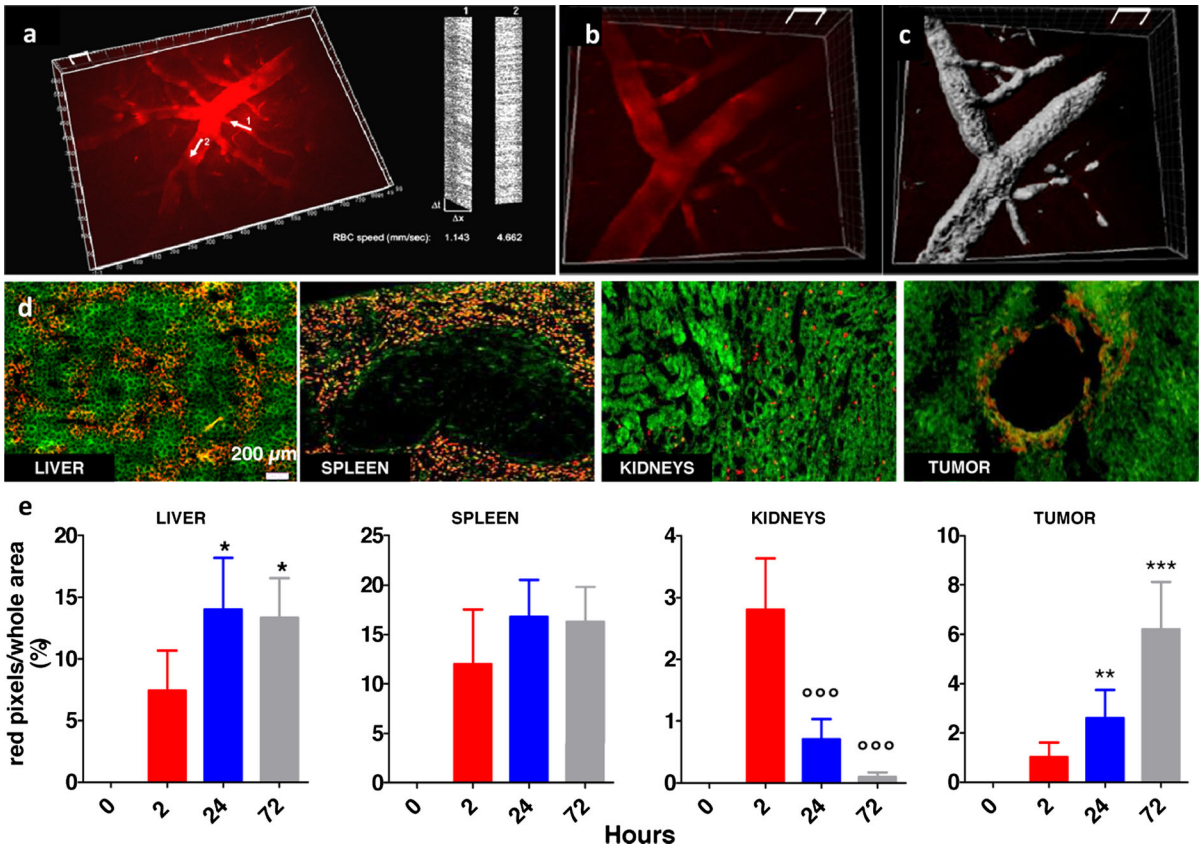

Fig. 6 **a**, **b** In vivo two-photon microscopy view of brain cortical vasculature 30′ (**a**) and 24 h (**b**) after PMMA-100^{+} injection. At both time-points vessels appeared in good shape and PMMA-100^{+} were found flowing in the bloodstream, even if after 24 h NP signal is much weaker. *Arrows* indicate the direction of flow and RBC speed was measured (1.143 mm/sec in small arterioles and 4.662 mm/sec in big pial vessels) 30′ after injection. Volume grid unit 50 μm. **c** 3D reconstruction from the fluorescent signal shown in panel **b**. **d** Representative confocal microscopy images showing sections of tissues in a mouse sacrificed 24 h after PMMA-100^{+} administration. PMMA-100^{+} signal is observed in *red*; in *green* autofluorescence is reported for anatomical detail. **e** Histogram showing the percentage area occupied by NP in tissues four different times after NP administration. Data are mean ± SE 10 sections from each tissue were processed and three animals were used for each experimental group. *Asterisk* (significant increase compared to the first time-point; *degree* (significant decrease compared to the first time-point). (Student's *t* test). (Color figure online)

injection into the bloodstream. In fact, it is known that the cellular and acelluar components of the blood might influence NP properties and regulate their fate (Baumann et al. 2013; Karmali and Simberg 2011). This is the case of plasma proteins that, interacting with NPs, form a protein layer on their surface called "protein corona" (Canovi et al. 2013). The occurrence of this phenomenon is highly related to NP dimensions and surface charge (Monopoli et al. 2012). Even if the present study was not aimed at further elucidating this process, we verified the influence of serum on NP stability. Our DLS, AFM, and fluorimetric data showed that all the tested NPs remained stable and monodispersed independently from their dimensions and charges even in presence of serum. These results allowed us to confirm the quality of NPs for further in vitro and in vivo steps.

To develop NPs against TNBC, where the absence of target receptors hinders extracellular pharmacological interactions, intracellular delivery of active compounds should be optimized. When evaluating the ability of our NPs to internalize into TNBC cell lines, we found that positively charged NPs have much more rapid kinetics and higher rate of internalization compared to negatively charged ones. This difference, which is probably due to the fact that opposite charges

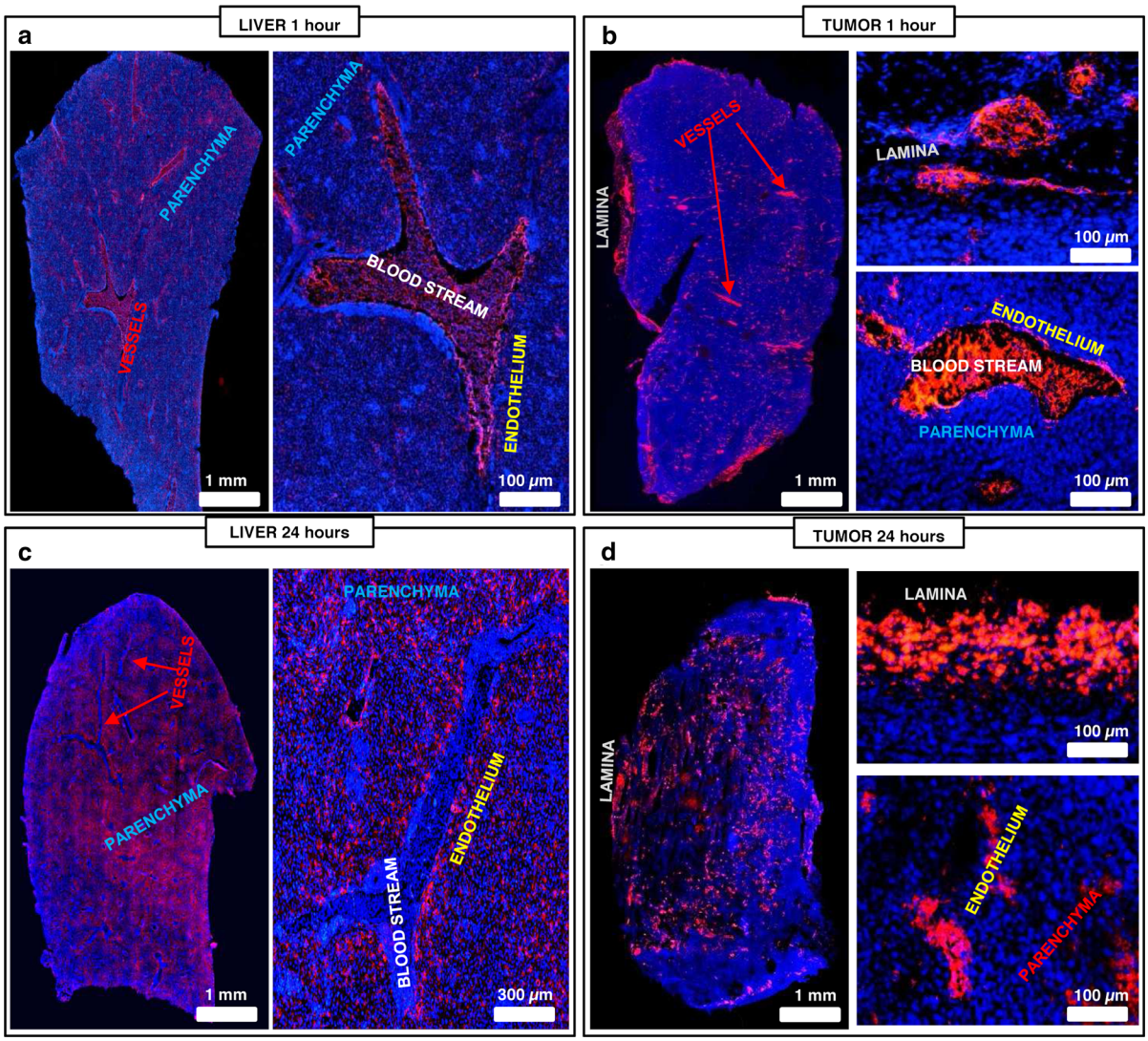

Fig. 7 Representative microscopy images showing the pattern of distribution of PMMA-100^{+} (*red signal*) in liver (**a**–**c**) and tumor (**b**–**d**) sections. In *blue*, Hoechst-33258 histological staining is visualized. One hour after NP systemic administration, PMMA-100^{+} are mainly located inside the blood vessels both in liver and in tumor, where they are also found on the external lamina. 24 h later, NPs seem to leave the bloodstream and actively migrate into tissue parenchyma. (Color figure online)

Table 1 First screening tests for NP selection

			PMMA 50^{+} (h)	PMMA 100^{+} (h)	PMMA 200^{+} (h)	PMMA 50^{-} (h)	PMMA 100^{-} (h)	PMMA 200^{-} (h)
In-silico	Stability		>48	>48	>48	>48	>48	>48
	Traceability over time		>48	>48	>48	>48	>48	>48
	Serum interaction		>48	>48	>48	>48	>48	>48
In vitro	Rate of internalization	4T1	Moderate	Very high	High	Very low	Very low	Low
		MDA	n.e.	High	n.e.	n.e.	n.e.	n.e.
	Growth inhibition	4T1	Low	Low	Low	n.e.	n.e.	n.e.
		MDA	Low	Moderate	Moderate	n.e.	n.e.	n.e.

Table 2 Characterization of the biological interactions for the selected PMMA-100^{+} NPs

In vitro	Apoptosis/necrosis	Cell cycle	Proliferation	Homeostasis perturbation	Subcellular localization	Vesicular transport
	MDA	MDA	MDA	MDA, 4T1	MDA, 4T1	MDA, 4T1
	Low	Low	Low	Absent	Perinuclear	Good >24 h
In vivo ex vivo	**Detectability in tissues and blood**	**Filter organs biodistribution**		**Accumulation**	**Clearance**	**Tumor penetration**
	Very good	Splenic, hepatic		Low	High	Moderate

between positive NPs and negative membrane favor reciprocal interactions (Ma et al. 2013) might help us in selecting proper NPs for future applications.

The penetration of NPs into the cytoplasm is a necessary condition to carry potential compounds in TNBC cells but it is not sufficient for account for a therapeutic response. Our high magnified images clearly revealed a spotty staining typical of endosomal compartmentalization of NPs. The retrieval transport of nanocarriers is a common receptor-independent mechanism for a wide range of NPs (Petros and DeSimone 2010). Here we showed that PMMA-NPs accumulate close to the perinuclear area but did not enter the nucleus. This localization is highly strategic thinking about a possible release of many chemoterapics or RNA-i based molecules (Malhotra et al. 2013). Our longitudinal characterization of subcellular organelles showed a selective activation of the lysosomal machinery from 24 to 48 h after NP exposure. This is an important suggestion to both demonstrate that even stable materials can be metabolized and to define a temporal window to be considered before developing biodegradable polymers for clinical purposes.

Even if the aim of NP-dependent drug delivery in TNBC is the death of target cells, the carrier must be safe when interacting with host tissues. Our data confirm the biocompatibility of PMMA-NPs, neither apoptosis/necrosis nor proliferation rate was found altered upon NP exposure. However, NP entry may also generate pathological effects that could be exacerbated by repeated administrations and chronic treatments. Our results confirmed that no relevant morphofunctional perturbation was observed regarding important parameters in TNBC following NP penetration. This body of evidence makes our platform an interesting tool for the evaluation of the main NP parameters in regulating the potential of polymeric NPs to be used as drug carriers against TNBC.

For a complete characterization in nanomedicine, in vitro studies should be completed with studies in both healthy and diseased animals. In vivo imaging in tumor bearing mice enabled us to demonstrate that NPs circulate into the bloodstream long enough to interact with different filter organs and tumors and are actually able to migrate from the blood to tissues parenchyma. To verify this, the contribution of NPs still circulating into the blood had to be eliminated and the measurement of extravasated NPs was carried out. By high resolution ex vivo histological analyses, we noticed that the peak of fluorescence of non-perfused tumors was revealed 24 h after injection. On the contrary, after removing blood, the fluorescent peak was observed after 72 h. This shift can be explained by the ability of NPs to migrate in tumor parenchyma. This happened also in liver and spleen, with much faster kinetics if compared to the tumors. By this result, it is possible to speculate that migration phenomena into these latter filter organs are regulated by active uptake mechanisms, while in tumors the accumulation of NPs is obtained through a passive EPR effect due to the leaky tumor vasculature.

In conclusion, the evaluation of stability, cellular uptake, safety, clearance activation, permanence in the bloodstream, and tumor tropism was considered as fundamental steps to fully characterize the interactions of "paradigmatic" polymeric NPs with their "therapeutic target." This platform was set up using PMMA-NPs because of their stability and was limited to the analysis of "nude fluorescent NPs." We believe that to define the safety of the material alone is the first step to plan a robust development of nanomaterials for therapeutic purposes. However, to develop reliable nanodrugs, biodegradable polymers should be used to enable the release of the loaded molecules. Obviously our evaluation does not exclude that these particles, if loaded with hazardous drugs, could potentially release them outside the target tumor and lead to systemic

toxicity. This issue should be carefully studied in future experiments. The system that was discussed here could be implemented when developing NPs loaded with candidate drugs. To test the release of the drugs, other screening methods could be easily integrated (such as by mass spectrometry and/or HPLC analyses) to the platform without changing the structure of the box. These improvements would represent other steps toward the optimization of a powerful instrument of analysis to fill the gap between basic science and clinical application.

Acknowledgments The authors are grateful to Mr. Ciprian Husanu and Dr. Rupert Ecker from TissueGnostics for technical help in quantification of fluorescent signals. A particular thanks to Dr. Laura Confalonieri, Dr. Stefano Pezzati, and Dr. Annamaria Mauro from Hamamatsu Photonics Italia for the support in acquiring images. L.S. is indebted to a private donor who is funding his research. The authors are grateful to AIRC for support for this research with the Special Program Molecular Clinical Oncology "5 per mille."

References

Akhter S, Ahmad I, Ahmad MZ, Ramazani F, Singh A, Rahman Z, Ahmad FJ, Storm G, Kok RJ (2013) Nanomedicines as cancer therapeutics: current status. Curr Cancer Drug Targets 13(4):362–378 CCDT-EPUB-20130318-1

Albani D, Polito L, Batelli S, De Mauro S, Fracasso C, Martelli G, Colombo L, Manzoni C, Salmona M, Caccia S, Negro A, Forloni G (2009) The SIRT1 activator resveratrol protects SK-N-BE cells from oxidative stress and against toxicity caused by alpha-synuclein or amyloid-beta (1-42) peptide. J Neurochem 110(5):1445–1456. doi:10.1111/j.1471-4159.2009.06228.x

Barenholz Y (2012) DoxilÂ® â€" The first FDA-approved nano-drug: lessons learned. J Control Release 160(2):117–134. doi:10.1016/j.jconrel.2012.03.020

Baumann D, Hofmann D, Nullmeier S, Panther P, Dietze C, Musyanovych A, Ritz S, Landfester K, Mailander V (2013) Complex encounters: nanoparticles in whole blood and their uptake into different types of white blood cells. Nanomedicine (Lond) 8(5):699–713. doi:10.2217/nnm.12.111

Bigini P, Previdi S, Casarin E, Silvestri D, Violatto MB, Facchin S, Sitia L, Rosato A, Zuccolotto G, Realdon N, Fiordaliso F, Salmona M, Morpurgo M (2013) In vivo fate of avidin-nucleic acid nanoassemblies as multifunctional diagnostic tools. ACS Nano. doi:10.1021/nn402669w

Canovi M, Lucchetti J, Stravalaci M, Re F, Moscatelli D, Bigini P, Salmona M, Gobbi M (2013) Applications of surface plasmon resonance (SPR) for the characterization of nanoparticles developed for biomedical purposes. Sensors (Basel) 12(12):16420–16432. doi:10.3390/s121216420

Cho EJ, Holback H, Liu KC, Abouelmagd SA, Park J, Yeo Y (2013) Nanoparticle characterization: state of the art, challenges, and emerging technologies. Mol Pharm 10(6):2093–2110. doi:10.1021/mp300697h

Cova L, Bigini P, Diana V, Sitia L, Ferrari R, Pesce RM, Khalaf R, Bossolasco P, Ubezio P, Lupi M, Tortarolo M, Colombo L, Giardino D, Silani V, Morbidelli M, Salmona M, Moscatelli D (2013) Biocompatible fluorescent nanoparticles for in vivo stem cell tracking. Nanotechnology 24(24):245603. doi:10.1088/0957-4484/24/24/245603

De Jong WH, Borm PJ (2008) Drug delivery and nanoparticles: applications and hazards. Int J Nanomed 3(2):133–149

de Ruijter TC, Veeck J, de Hoon JP, van Engeland M, Tjan-Heijnen VC (2011) Characteristics of triple-negative breast cancer. J Cancer Res Clin Oncol 137(2):183–192. doi:10.1007/s00432-010-0957-x

Deng ZJ, Morton SW, Ben-Akiva E, Dreaden EC, Shopsowitz KE, Hammond PT (2013) Layer-by-layer nanoparticles for systemic codelivery of an anticancer drug and siRNA for potential triple-negative breast cancer treatment. ACS Nano 7(11):9571–9584. doi:10.1021/nn4047925

Dobrovolskaia MA, McNeil SE (2013) Understanding the correlation between in vitro and in vivo immunotoxicity tests for nanomedicines. J Control Release 172(2):456–466. doi:10.1016/j.jconrel.2013.05.025

Dossi M, Ferrari R, Dragoni L, Martignoni C, Gaetani P, D'Incalci M, Morbidelli M, Moscatelli D (2012) Synthesis of fluorescent PMMA-based nanoparticles. Macromol Mater Eng 298(7):771–778. doi:10.1002/mame.201200122

Ferrari R, Lupi M, Falcetta F, Bigini P, Paolella K, Fiordaliso F, Bisighini C, Salmona M, D'Incalci M, Morbidelli M, Moscatelli D, Ubezio P (2014) Integrated multiplatform method for in vitro quantitative assessment of cellular uptake for fluorescent polymer nanoparticles. Nanotechnology 25(4):045102. doi:10.1088/0957-4484/25/4/045102

Fumagalli S, Coles JA, Ejlerskov P, Ortolano F, Bushell TJ, Brewer JM, De Simoni MG, Dever G, Garside P, Maffia P, Carswell HV (2011) In vivo real-time multiphoton imaging of T lymphocytes in the mouse brain after experimental stroke. Stroke 42(5):1429–1436. doi:10.1161/STROKEAHA.110.603704

Fumagalli S, Perego C, Ortolano F, De Simoni MG (2013) CX3CR1 deficiency induces an early protective inflammatory environment in ischemic mice. Glia 61(6):827–842. doi:10.1002/glia.22474

Inoue S, Patil R, Portilla-Arias J, Ding H, Konda B, Espinoza A, Mongayt D, Markman JL, Elramsisy A, Phillips HW, Black KL, Holler E, Ljubimova JY (2012) Nanobiopolymer for direct targeting and inhibition of EGFR expression in triple negative breast cancer. PLoS One 7(2):e31070. doi:10.1371/journal.pone.0031070

Karmali PP, Simberg D (2011) Interactions of nanoparticles with plasma proteins: implication on clearance and toxicity of drug delivery systems. Expert Opin Drug Deliv 8(3):343–357. doi:10.1517/17425247.2011.554818

Liechty WB, Peppas NA (2012) Expert opinion: responsive polymer nanoparticles in cancer therapy. Eur J Pharm Biopharm 80(2):241–246. doi:10.1016/j.ejpb.2011.08.004

Ma P, Mumper RJ (2013) Paclitaxel nano-delivery systems: a comprehensive review. J Nanomed Nanotechnol 4(2):1000164. doi:10.4172/2157-7439.1000164

Ma N, Ma C, Li C, Wang T, Tang Y, Wang H, Moul X, Chen Z, Hel N (2013) Influence of nanoparticle shape, size, and

surface functionalization on cellular uptake. J Nanosci Nanotechnol 13(10):6485–6498

Malam Y, Loizidou M, Seifalian AM (2009) Liposomes and nanoparticles: nanosized vehicles for drug delivery in cancer. Trends Pharmacol Sci 30(11):592–599. doi:10.1016/j.tips.2009.08.004

Malhotra M, Tomaro-Duchesneau C, Saha S, Kahouli I, Prakash S (2013) Development and characterization of chitosan–PEG–TAT nanoparticles for the intracellular delivery of siRNA. Int J Nanomed 8:2041–2052. doi:10.2147/IJN.S43683

Matsumura Y (2008) Polymeric micellar delivery systems in oncology. Jpn J Clin Oncol 38(12):793–802. doi:10.1093/jjco/hyn116

Monopoli MP, Aberg C, Salvati A, Dawson KA (2012) Biomolecular coronas provide the biological identity of nanosized materials. Nat Nanotechnol 7(12):779–786. doi:10.1038/nnano.2012.207

Mukerjee A, Ranjan AP, Vishwanatha JK (2012) Combinatorial nanoparticles for cancer diagnosis and therapy. Curr Med Chem 19(22):3714–3721 CMC-EPUB-20120607-22 [pii]

Nazir S, Hussain T, Ayub A, Rashid U, Macrobert AJ (2014) Nanomaterials in combating cancer: therapeutic applications and developments. Nanomedicine 10(1):19–34. doi:10.1016/j.nano.2013.07.001

Pal SK, Childs BH, Pegram M (2011) Triple negative breast cancer: unmet medical needs. Breast Cancer Res Treat 125(3):627–636. doi:10.1007/s10549-010-1293-1

Parveen S, Misra R, Sahoo SK (2011) Nanoparticles: a boon to drug delivery, therapeutics, diagnostics and imaging. Nanomedicine 8(2):147–166. doi:10.1016/j.nano.2011.05.016

Peer D, Karp JM, Hong S, Farokhzad OC, Margalit R, Langer R (2007) Nanocarriers as an emerging platform for cancer therapy. Nat Nanotechnol 2(12):751–760. doi:10.1038/nnano.2007.387

Petros RA, DeSimone JM (2010) Strategies in the design of nanoparticles for therapeutic applications. Nat Rev Drug Discov 9(8):615–627. doi:10.1038/nrd2591

Schaffer CB, Friedman B, Nishimura N, Schroeder LF, Tsai PS, Ebner FF, Lyden PD, Kleinfeld D (2006) Two-photon imaging of cortical surface microvessels reveals a robust redistribution in blood flow after vascular occlusion. PLoS Biol 4(2):e22. doi:10.1371/journal.pbio.0040022

Wang AZ, Langer R, Farokhzad OC (2011) Nanoparticle delivery of cancer drugs. Annu Rev Med 63:185–198. doi:10.1146/annurev-med-040210-162544

Yang Z, Kang SG, Zhou R (2013) Nanomedicine: de novo design of nanodrugs. Nanoscale 6(2):663–677. doi:10.1039/c3nr04535h